Efficient On-the-Fly Interpolation Technique for Bethe-Salpeter Calculations of Optical Spectra

Yannick Gillet[a,*], Matteo Giantomassi[a], Xavier Gonze[a]

[a] *European Theoretical Spectroscopy Facility, Institute of Condensed Matter and Nanosciences, Université catholique de Louvain, Chemin des étoiles 8, bte L7.03.01, 1348 Louvain-la-Neuve, Belgium*

Abstract

The Bethe-Salpeter formalism represents the most accurate method available nowadays for computing neutral excitation energies and optical spectra of crystalline systems from first principles. Bethe-Salpeter calculations yield very good agreement with experiment but are notoriously difficult to convergence with respect to the sampling of the electronic wavevectors. Well-converged spectra therefore require significant computational and memory resources, even by today's standards. These bottlenecks hinder the investigation of systems of great technological interests and also render difficult the study of derived quantities like piezoreflectance, thermoreflectance or resonant Raman intensities.

We present a new methodology that decreases the workload needed to reach a given accuracy. It is based on a double-grid on-the-fly interpolation within the Brillouin zone, combined with the Lanczos algorithm. It achieves significant speed-up and reduction of memory requirements. The technique is benchmarked in terms of accuracy on silicon, gallium arsenide and lithium fluoride. The performance of the method is studied from low to very-high density of points in the Brillouin Zone, showing a much better scaling than a conventional implementation. We also compare our method with other similar techniques proposed in the literature.

1. Introduction

The calculation of optical properties from first principles can be achieved with different levels of approximation and different computational requirements. The Bethe-Salpeter Equation (BSE) in the framework of Many-Body Perturbation Theory is the most precise and sophisticated approach to compute the macroscopic dielectric function including the attractive electron-hole interaction [1]. This formalism has been used since 1998 [2] for the first-principles computation of the optical spectra of semiconductors and insulators. Even if its

*Corresponding author.
E-mail address: yannick.gillet@uclouvain.be

application to simple materials is reasonably frequent nowadays, the calculation of optical properties of complex materials with more than two dozen of atoms in the unit cells is still challenging (see e.g. the work of Kresse *et al.* [3] and Rinke *et al.* [4]). Algorithmic improvements [5, 6, 7, 8], and new theoretical developments to introduce temperature dependence [9], or to compute resonant Raman intensities from derivatives of optical response [10] are active domains of research.

Independently of the approximations used, the precise description of the dielectric properties usually requires a large number of wavevectors to sample the Brillouin Zone (BZ). Each wavevector of the BZ, indeed, gives contributions at different transition energies and small changes in the mesh density can induce oscillations in the dielectric properties [10]. The construction of the BSE Hamiltonian requires the computation of matrix elements connecting different points in the wavevector mesh. This computation is the most time-consuming part of the BSE flow and its cost renders well-converged results difficult to achieve. The extraction of the macroscopic dielectric function from the inversion of the Hamiltonian matrix constitutes the last step of the BSE flow. Two different approaches are commonly used nowadays: direct diagonalization and Lanczos algorithms following the seminal work of Haydock [11]. The Lanczos approach was employed for the first time to the solution of the BSE by Benedict *et al.* [12, 13], and it is based on the construction of a chain of vectors obtained by performing simple matrix-vector operations.

Since 1998, different numerical methods have been proposed to help reducing the computational cost. Rohlfing and Louie [5] (abbreviated RL) proposed a double-grid technique where the kernel is interpolated starting from a homogeneous coarse mesh. This approach is used, for example, in the BerkeleyGW code [14]. Another technique by Fuchs *et al.* [15], uses an inhomogeneous mesh and refines the sampling to extract specific information for bound excitons. The large Hamiltonian matrices obtained with these methods are then treated either by direct diagonalization or with the Lanczos algorithm. Alternatively, one can perform the average of optical properties using several independent shifted coarse grids, as introduced by Paier *et al.* [6] and, later, by Gillet *et al.* [10].

A completely different approach to the BSE problem has been proposed recently by Kammerländer *et al.* [16]. The authors focus on a single frequency and avoid the setup of the entire matrix and the direct diagonalization by using an iterative technique that takes advantage of a double grid to solve the Dyson equation.

In the present work, we propose a new method that combines the RL interpolation with the Lanczos-Haydock algorithm without requiring the storage of the full matrix. We also generalize the RL approach to include multi-linear interpolation, and we reformulate the algorithm to render it more scalable and less memory demanding. We present different levels of interpolation, with different computational loads.

This article is organized as follows. In Section 2, we describe the main equations and the iterative approach used to solve the BSE. Section 3 presents

the interpolation methodology while the technical details of the implementation are discussed in Section 4. Finally, in Section 5, we apply our technique with different interpolation levels to three different crystalline systems: bulk silicon, gallium arsenide and lithium fluoride. We conclude with a comparison between our method and other similar techniques proposed by Paier *et al.* [6] and Gillet *et al.* [10], and the work of Kammerländer *et al.* [16].

2. The Bethe-Salpeter Equation and the Lanczos recursion algorithm

In the so-called Tamm-Dancoff Approximation (TDA) [17], the matrix elements of the BSE Hamiltonian in the transition space, i.e. products of valence and conduction bands, are given by

$$H_{vc\boldsymbol{k},v'c'\boldsymbol{k}'} = (\varepsilon_{c\boldsymbol{k}} - \varepsilon_{v\boldsymbol{k}})\,\delta_{\boldsymbol{k}\boldsymbol{k}'}\delta_{vv'}\delta_{cc'} + K_{vc\boldsymbol{k},v'c'\boldsymbol{k}'}, \tag{1}$$

where the kernel K is defined as

$$K_{vc\boldsymbol{k},v'c'\boldsymbol{k}'} = 2\left\langle vc\boldsymbol{k}\left|\bar{v}\right|v'c'\boldsymbol{k}'\right\rangle - \left\langle vc\boldsymbol{k}\left|W\right|v'c'\boldsymbol{k}'\right\rangle, \tag{2}$$

with

$$\langle vc\mathbf{k}\left|\bar{v}\right|v'c'\mathbf{k}\rangle = \int\int \psi_{v\mathbf{k}}(\mathbf{r})\psi^*_{c\mathbf{k}}(\mathbf{r})\bar{v}(\mathbf{r}-\mathbf{r}')\psi^*_{v'\mathbf{k}'}(\mathbf{r}')\psi_{c'\mathbf{k}'}(\mathbf{r}')d\mathbf{r}'d\mathbf{r} \tag{3}$$

$$\left\langle vc\mathbf{k}\left|W\right|v'c'\mathbf{k}'\right\rangle = \int\int \psi_{v\mathbf{k}}(\mathbf{r})\psi^*_{v'\mathbf{k}'}(\mathbf{r})W(\mathbf{r},\mathbf{r}')\psi^*_{c\mathbf{k}}(\mathbf{r}')\psi_{c'\mathbf{k}'}(\mathbf{r}')d\mathbf{r}'d\mathbf{r}. \tag{4}$$

In the above expressions, v and c stands for valence and conduction band indices, $\mathbf{k}$ is a wavevector in the BZ, $\varepsilon_{n\mathbf{k}}$ and $\psi_{n\mathbf{k}}$ are the energies and wavefunctions of band n at point $\mathbf{k}$. Equation (3) represents the so-called exchange term and takes into account local-fields effects. $\bar{v}$ is a modified bare Coulomb potential obtained from the bare potential $v(\boldsymbol{G})$ by setting the $\boldsymbol{G} = 0$ component to zero. The expression in Eq.(4) is usually referred to as the direct term and takes into account the static screened Coulomb interaction, W, through the inverse dielectric function $\epsilon^{-1}(\mathbf{r},\mathbf{r}')$ via

$$W(\mathbf{r},\mathbf{r}') = \int d\mathbf{r}''\epsilon^{-1}(\mathbf{r},\mathbf{r}'')v(\mathbf{r}''-\mathbf{r}'), \tag{5}$$

The wavefunctions and eigenenergies are usually obtained from a standard Kohn-Sham calculation [18, 19] and a scissors operator may be employed to mimic the opening of the gap introduced by the GW approximation [1]. For BSE applications, it is common to compute the direct term with a screened interaction obtained within the Random-Phase Approximation (RPA) [20, 21]. Alternatively, one can employ the much cheaper model dielectric function proposed by Cappellini in Ref. [22].

Finally, the macroscopic dielectric function $\varepsilon_M(\omega)$ is given by

$$\varepsilon_M(\omega) = 1 - \lim_{\boldsymbol{q}\to 0} v(\boldsymbol{q})\left\langle P(\boldsymbol{q})\left|((\omega+i\eta)-H)^{-1}\right|P(\boldsymbol{q})\right\rangle \tag{6}$$

where $v(\boldsymbol{q})$ is the Fourier transform of the Coulomb interaction, $P(\boldsymbol{q})$ are the oscillator matrix elements

$$P(\boldsymbol{q})_{vc\boldsymbol{k}} = \left\langle c\boldsymbol{k}+\boldsymbol{q} \left| e^{i\boldsymbol{q}.\boldsymbol{r}} \right| v\boldsymbol{k} \right\rangle \tag{7}$$

evaluated for small $\boldsymbol{q}$ and η is a broadening factor.

The solution of the Bethe-Salpeter equation is a two-step process. First, the matrix elements of the Hamiltonian are computed from Eqs. (1-4). Then, the macroscopic dielectric function is derived using Eq. (6).

In order to avoid the inversion of large matrices, Lanczos-based iterative techniques (called Lanczos algorithm in this work) can be used to obtain the macroscopic dielectric function. By using Krylov subspaces, it is possible to express Eq. (6) in terms of a continued fraction formula.

The Lanczos algorithm can be summarized as follows. We start by setting

$$b_1 = 0 \tag{8}$$

$$|\psi_1\rangle = \frac{|P(\boldsymbol{q})\rangle}{\| \, |P(\boldsymbol{q})\rangle \, \|}. \tag{9}$$

Then the algorithm iterates with i starting at 1

$$a_i = \langle \psi_i | H | \psi_i \rangle \tag{10}$$

$$b_{i+1} = \| H|\psi_i\rangle - a_i|\psi_i\rangle - b_i|\psi_{i-1}\rangle \| \tag{11}$$

$$|\psi_{i+1}\rangle = \frac{H|\psi_i\rangle - a_i|\psi_i\rangle - b_i|\psi_{i-1}\rangle}{b_{i+1}}. \tag{12}$$

The frequency dependence of the dielectric function is computed in an efficient way in terms of the continued fraction

$$\varepsilon_M(\omega) = 1 - \lim_{\boldsymbol{q}\to 0} v(\boldsymbol{q}) \frac{\|P(\boldsymbol{q})\|^2}{(\omega+i\eta) - a_1 - \frac{b_2^2}{(\omega+i\eta)-a_2-\frac{b_3^2}{\cdots}}} \tag{13}$$

and the iteration is stopped when $\varepsilon_M(\omega)$ is converged for each frequency.

The construction of the Krylov chain Eqs. (10-12) requires only the application of the Hamiltonian on different functions or, in linear algebra language, simple matrix-vector products. The computational cost scales as $\mathcal{O}(mN^2)$ with m the number of iterations of the Lanczos algorithm and N the dimension of the matrix. In our approach, the BSE Hamiltonian is expressed in the electron-hole basis thus $N = N_v N_c N_k$ where N_v is the number of valence bands, N_c the number of conduction bands and N_k the number of points in the BZ.

The number of iterations m needed to converge $\varepsilon_M(\omega)$ is much smaller than the size of the Hamiltonian and almost independent of the size of the system. As a consequence, Lanczos methods are much more efficient than direct diagonalization techniques that scale as $\mathcal{O}(N^3)$. Unfortunately, unlike diagonalization methods, the Lanczos approach does not give direct access to the exciton levels and the corresponding wavefunctions.

The computation of the BSE matrix elements and the storage of the Hamiltonian represent the most CPU-intensive and memory demanding parts. For example, a converged computation of the dielectric function of bulk silicon requires few bands (3-4 valence bands, 4-6 conduction bands) but a large number of wavevectors in the BZ (from 14×14×14 to 40×40×40, depending on the accuracy required) which means that ca. 10^3 to 10^4 wavevectors must be sampled. This gives, for sequential computers, from days to years of computation, and in terms of memory, matrices of size ranging from 32928×32928 (ca. 16 GB) to 1536000×1536000 (ca. 34 TB). Such huge amount of memory and the corresponding computation time render BSE calculations challenging even on modern supercomputers. These issues are even more severe when BSE results are used to perform resonant Raman scattering calculations that, as illustrated in Ref. [10], require an exceedingly dense BZ sampling.

These two bottlenecks can be reduced by using the technique presented in the next section.

3. Presentation of the interpolation technique

The interpolation scheme we propose is based on two meshes of wavevectors in the BZ (double-grid technique). Later, we will distinguish different levels of interpolation, all based on this double-grid technique.

To facilitate the discussion, we introduce the following notation. The coarse mesh contains $\tilde{N}_k$ homogeneous wavevectors, denoted as $\tilde{\boldsymbol{k}}$. The dense mesh contains $N_k = \tilde{N}_k \times N_{div}$ homogeneous wavevectors obtained by refining the coarse mesh. The refining in each direction is done by defining equally spaced n_i points in the i-th direction. The wavevectors of the coarse mesh are given by

$$\tilde{\boldsymbol{k}}_{(i_1,i_2,i_3)} = i_1\hat{\boldsymbol{k}}_1 + i_2\hat{\boldsymbol{k}}_2 + i_3\hat{\boldsymbol{k}}_3, \tag{14}$$

where i_j are integer coordinates and $\hat{\boldsymbol{k}}_j$ are the basis vectors of the coarse mesh.

The dense wavevectors have fractional coordinates

$$\boldsymbol{k}_{(i_1,i_2,i_3),(j_1,j_2,j_3)} = (i_1 + \frac{j_1}{n_1})\hat{\boldsymbol{k}}_1 + (i_2 + \frac{j_2}{n_2})\hat{\boldsymbol{k}}_2 + (i_3 + \frac{j_3}{n_3})\hat{\boldsymbol{k}}_3 \tag{15}$$

where n_1, n_2 and n_3 are the number of divisions along the basis vectors while $0 \leq j_i \leq (n_i - 1)$. For the sake of simplicity, we assume the same number of divisions, $n_1 = n_2 = n_3 = n_{div}$, along the three directions and therefore $N_{div} = n_{div}^3$.

The neighborhood of a dense point, $N(\boldsymbol{k})$, is defined as the set of the eight wavevectors around $\boldsymbol{k}$. The reduced coordinates of this set of points are given by

$$N(\boldsymbol{k}_{(i_1,i_2,i_3),(j_1,j_2,j_3)}) = \left\{\tilde{\boldsymbol{k}}^{lmn}_{(i_1,i_2,i_3),(j_1,j_2,j_3)}\right\} \text{ with } l,m,n = 0,1 \tag{16}$$

where $\tilde{\boldsymbol{k}}^{lmn}$ is the lmn^{th}-neighbor of $\boldsymbol{k}$

$$\tilde{\boldsymbol{k}}^{lmn}_{(i_1,i_2,i_3),(j_1,j_2,j_3)} = \tilde{\boldsymbol{k}}_{(i_1+l,i_2+m,i_3+n)}. \tag{17}$$

The dense set of a coarse point, $S(\tilde{\boldsymbol{k}})$, is defined as

$$S(\tilde{\boldsymbol{k}}_{(i_1,i_2,i_3)}) = \left\{\boldsymbol{k}_{(i_1,i_2,i_3),(j_1,j_2,j_3)}\right\} \forall (j_1,j_2,j_3). \tag{18}$$

Using these definitions, we can derive the following important relation

$$\begin{aligned}\sum_{\boldsymbol{k}} \sum_{\tilde{\boldsymbol{k}}\in N(\boldsymbol{k})} f(\boldsymbol{k},\tilde{\boldsymbol{k}}) &= \sum_{\tilde{\boldsymbol{k}}'} \sum_{\boldsymbol{k}\in S(\tilde{\boldsymbol{k}}')} \sum_{\tilde{\boldsymbol{k}}\in N(\boldsymbol{k})} f(\boldsymbol{k},\tilde{\boldsymbol{k}}) \\ &= \sum_{\tilde{\boldsymbol{k}}'} \sum_{\boldsymbol{k}\in S(\tilde{\boldsymbol{k}}')} \sum_{\tilde{\boldsymbol{k}}\in N(\tilde{\boldsymbol{k}}')} f(\boldsymbol{k},\tilde{\boldsymbol{k}}) \\ &= \sum_{\tilde{\boldsymbol{k}}'} \sum_{\tilde{\boldsymbol{k}}\in N(\tilde{\boldsymbol{k}}')} \sum_{\boldsymbol{k}\in S(\tilde{\boldsymbol{k}}')} f(\boldsymbol{k},\tilde{\boldsymbol{k}})\end{aligned} \tag{19}$$

where Eq. (16) has been used. This property will be used afterwards to perform the interpolation of data defined on the coarse mesh.

As discussed in the previous section, the Lanczos algorithm is based on matrix-vector products. In our method, we perform these operations on-the-fly to avoid the storage of the BSE Hamiltonian in memory. The matrix elements of the kernel are interpolated while performing the matrix-vector operations. As discussed in more detail in the next paragraphs, different levels of interpolation can be employed in this part of the algorithm.

Since the periodic parts of the Bloch states at a given wavevector form a complete basis set, any wavefunction on the dense mesh can be expressed as [5]

$$|u_{n\boldsymbol{k}}\rangle = \sum_{n'} d_{n\boldsymbol{k}}^{n'\tilde{\boldsymbol{k}}} \left|u_{n'\tilde{\boldsymbol{k}}}\right\rangle \tag{20}$$

where

$$d_{n\boldsymbol{k}}^{n'\tilde{\boldsymbol{k}}} = \left\langle u_{n'\tilde{\boldsymbol{k}}} \middle| u_{n\boldsymbol{k}} \right\rangle . \tag{21}$$

In the transition basis set, the electron-hole wavefunction $\Psi(\boldsymbol{r},\boldsymbol{r}')$ is given by a linear combination of products of single-particle orbitals according to

$$\Psi(\boldsymbol{r},\boldsymbol{r}') = \sum_{vc\boldsymbol{k}} A_{vc\boldsymbol{k}} \phi_{vc\boldsymbol{k}}(\boldsymbol{r},\boldsymbol{r}') \tag{22}$$

where

$$\phi_{vc\boldsymbol{k}}(\boldsymbol{r},\boldsymbol{r}') = e^{-i\boldsymbol{k}.\boldsymbol{r}} u_{v\boldsymbol{k}}^*(\boldsymbol{r}) e^{i\boldsymbol{k}.\boldsymbol{r}'} u_{c\boldsymbol{k}}(\boldsymbol{r}') = e^{i\boldsymbol{k}.(\boldsymbol{r}'-\boldsymbol{r})} U_{vc\boldsymbol{k}}(\boldsymbol{r},\boldsymbol{r}'). \tag{23}$$

One basis function on the dense mesh can then be expanded in term of the wavefunctions located on a coarse point by means of

$$|U_{vc\boldsymbol{k}}\rangle = \sum_{n_1 n_2} (d_{v\boldsymbol{k}}^{n_1\tilde{\boldsymbol{k}}})^* d_{c\boldsymbol{k}}^{n_2\tilde{\boldsymbol{k}}} \left|U_{n_1 n_2 \tilde{\boldsymbol{k}}}\right\rangle . \tag{24}$$

The method developed by Rohlfing and Louie in Ref. [5] uses a single reference point $\tilde{\boldsymbol{k}}$ to expand the kernel according to

$$K^i_{vc\boldsymbol{k},v'c'\boldsymbol{k}'} = \sum_{n_1 n_2} d^{n_1\tilde{\boldsymbol{k}}}_{v\boldsymbol{k}} (d^{n_2\tilde{\boldsymbol{k}}}_{c\boldsymbol{k}})^* \sum_{n_3 n_4} (d^{n_3\tilde{\boldsymbol{k}}'}_{v'\boldsymbol{k}'})^* d^{n_4\tilde{\boldsymbol{k}}'}_{c'\boldsymbol{k}'} K_{n_1 n_2\tilde{\boldsymbol{k}},n_3 n_4\tilde{\boldsymbol{k}}'} \tag{25}$$

and we generalize their approach by including eight coarse points in the expansion of the wavefunctions

$$|U_{vc\boldsymbol{k}}\rangle = \sum_{\tilde{\boldsymbol{k}}\in N(\boldsymbol{k})} f(\boldsymbol{k},\tilde{\boldsymbol{k}}) \sum_{n_1 n_2} (d^{n_1\tilde{\boldsymbol{k}}}_{v\boldsymbol{k}})^* d^{n_2\tilde{\boldsymbol{k}}}_{c\boldsymbol{k}} |U_{n_1 n_2\tilde{\boldsymbol{k}}}\rangle \ , \tag{26}$$

where $f(\boldsymbol{k},\tilde{\boldsymbol{k}})$ are interpolation prefactors. The RL interpolation scheme is a special case of Eq. (26) in which $f(\boldsymbol{k},\tilde{\boldsymbol{k}}) = 1$ for a chosen neighbor and 0 for all the other ones.

In order to accelerate the convergence of the expansion, we perform a trilinear interpolation of the coefficients. In this case, the prefactors are given by

$$\begin{aligned} f(\boldsymbol{k},\tilde{\boldsymbol{k}}) &= 0 \qquad\qquad \text{if } \tilde{\boldsymbol{k}} \notin N(\boldsymbol{k}) \\ f(\boldsymbol{k},\tilde{\boldsymbol{k}}^{lmn}) &= f^{lmn}_{\boldsymbol{k}_{(i_1,i_2,i_3),(j_1,j_2,j_3)}} = f^l_{j_1} f^m_{j_2} f^n_{j_3} \end{aligned} \tag{27}$$

with

$$f^l_j = \begin{cases} 1 - \dfrac{j}{n_{div}} \text{ if } l = 0 \\ \dfrac{j}{n_{div}} \text{ if } l = 1. \end{cases} \tag{28}$$

Using Eq. (26), one obtains the following expression for the interpolated matrix elements

$$K^i_{vc\boldsymbol{k},v'c'\boldsymbol{k}'} = \sum_{\tilde{\boldsymbol{k}}\in N(\boldsymbol{k})} f(\boldsymbol{k},\tilde{\boldsymbol{k}}) \sum_{n_1 n_2} d^{n_1,\tilde{\boldsymbol{k}}}_{v\boldsymbol{k}} (d^{n_2\tilde{\boldsymbol{k}}}_{c\boldsymbol{k}})^* \sum_{\tilde{\boldsymbol{k}}'\in N(\boldsymbol{k}')} f(\boldsymbol{k}',\tilde{\boldsymbol{k}}') \sum_{n_3 n_4} (d^{n_3\tilde{\boldsymbol{k}}'}_{v'\boldsymbol{k}'})^* d^{n_4\tilde{\boldsymbol{k}}'}_{c'\boldsymbol{k}'} K_{n_1 n_2\tilde{\boldsymbol{k}},n_3 n_4\tilde{\boldsymbol{k}}'}. \tag{29}$$

By using the overlaps of the periodic parts of the wavefunctions, we are thus able to include correctly the phases of the wavefunctions and these phases will cancel out with the oscillator matrix elements $P(\boldsymbol{q})$ computed with the wavefunctions on the dense mesh.

It should be stressed, however, that the matrix elements of the Coulomb interaction diverge when $\boldsymbol{q} = \boldsymbol{k} - \boldsymbol{k}' \to 0$. Following Ref. [5], we rewrite the matrix elements as

$$K_{vc\boldsymbol{k},v'c'\boldsymbol{k}'} = \frac{a_{vc\boldsymbol{k},v'c'\boldsymbol{k}'}}{\boldsymbol{q}^2} + \frac{b_{vc\boldsymbol{k},v'c'\boldsymbol{k}'}}{\boldsymbol{q}} + c_{vc\boldsymbol{k},v'c'\boldsymbol{k}'} \tag{30}$$

and we note that an accurate interpolation technique should try to reproduce the divergent behavior as much as possible.

The different schemes we have implemented to treat the divergence are discussed in more detail in the next section.

4. Combining Lanczos algorithm with interpolation

As previously discussed, the dimension of the matrix on the coarse mesh is $N_{coarse} = N_c N_v \tilde{N}_k$, while the dimension of the matrix on the dense mesh is $N_{dense} = N_c N_v N_k = N_c N_v \tilde{N}_k N_{div}$. The calculation of the matrix elements of the Hamiltonian as well as the Lanczos algorithm scale as $\mathcal{O}(N^2)$. The numerical complexity of the standard BSE solution on the coarse mesh is thus

$$\mathcal{O}(N_c^2 N_v^2 \tilde{N}_k^2) \tag{31}$$

while the complete solution on the dense mesh scales as

$$\mathcal{O}(N_c^2 N_v^2 \tilde{N}_k^2 N_{div}^2). \tag{32}$$

To fix the ideas, supposing a halving of the coarse mesh for the three directions giving the dense mesh, $N_{div} = 8$ and $N_{div}^2 = 64$, which points out the significant burden of using the dense meshes. If $\tilde{N}_k$ is kept constant, and N_{div} is increased, the use of the dense mesh is even more unfavorable.

The most memory-demanding part is the storage of the Hamiltonian which scales quadratically with the size of the Hamiltonian. The interpolation technique given in Eq. (29) can be implemented in two different ways. The interpolated matrix elements can be stored in memory and then used as a standard matrix for the Lanczos technique. This is the approach followed by Rohlfing in [5]. It is worth noting, however, that although the RL method allows one to avoid the explicit computation of the matrix elements on the dense mesh, the numerical complexity and the memory requirements of the approach are still the ones of a standard BSE.

Alternatively, one can reformulate the equations so that the interpolation is done on-the-fly without allocating extra memory for the dense Hamiltonian. This is the central result of this paper. As the Lanczos technique requires only matrix-vector multiplications, the full-matrix vector multiplication with the Hamiltonian can be written as

$$\phi^{(n+1)}_{vc\boldsymbol{k}} = \sum_{v'c'\boldsymbol{k}'} H^i_{vc\boldsymbol{k},v'c'\boldsymbol{k}'} \phi^{(n)}_{v'c'\boldsymbol{k}'} \tag{33}$$

$$= (\varepsilon_{c\boldsymbol{k}} - \varepsilon_{v\boldsymbol{k}})\, \phi^{(n)}_{vc\boldsymbol{k}} + \sum_{v'c'\boldsymbol{k}'} K^i_{vc\boldsymbol{k},v'c'\boldsymbol{k}'} \phi^{(n)}_{v'c'\boldsymbol{k}'} \tag{34}$$

that can be computed with $\mathcal{O}(N_c N_v \tilde{N}_k N_{div})$ scaling. The matrix-vector product

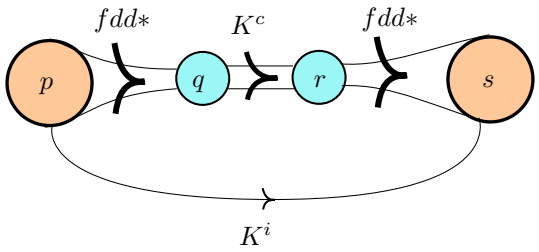

Figure 1: Color online. Schema illustrating the interpolated matrix-vector product. Small circles represent coarse mesh data while big circles correspond to dense mesh data. $fdd*$ refers to the $f(\boldsymbol{k},\tilde{\boldsymbol{k}})d_{v\boldsymbol{k}}^{n_1,\tilde{\boldsymbol{k}}}(d_{c\boldsymbol{k}}^{n_2\tilde{\boldsymbol{k}}})^*$ prefactors of Eq. (37) and Eq. (39). K_c is the application of the coarse kernel on the coarse vector q that gives r in Eq. (38).

with the kernel can be rewritten as

$$s_{vc\boldsymbol{k}} = \sum_{v'c'\boldsymbol{k}'} K^i_{vc\boldsymbol{k},v'c'\boldsymbol{k}'} p_{v'c'\boldsymbol{k}'} \tag{35}$$

$$\begin{aligned} &= \sum_{\tilde{\boldsymbol{k}}\in N(\boldsymbol{k})} f(\boldsymbol{k},\tilde{\boldsymbol{k}}) \sum_{n_1n_2} d_{v\boldsymbol{k}}^{n_1,\tilde{\boldsymbol{k}}}(d_{c\boldsymbol{k}}^{n_2\tilde{\boldsymbol{k}}})^* \\ &\quad \sum_{\tilde{\boldsymbol{k}}''} \sum_{\tilde{\boldsymbol{k}}'\in N(\tilde{\boldsymbol{k}}'')} \sum_{n_3n_4} K_{n_1n_2\tilde{\boldsymbol{k}},n_3n_4\tilde{\boldsymbol{k}}'} \\ &\quad \sum_{\boldsymbol{k}'\in S(\tilde{\boldsymbol{k}}'')} f(\boldsymbol{k}',\tilde{\boldsymbol{k}}') \sum_{v'c'} (d_{v'\boldsymbol{k}'}^{n_3\tilde{\boldsymbol{k}}'})^* d_{c'\boldsymbol{k}'}^{n_4\tilde{\boldsymbol{k}}'} p_{v'c'\boldsymbol{k}'}. \end{aligned} \tag{36}$$

and can be computed in three steps using

$$q^{uvw}_{n_3n_4\tilde{\boldsymbol{k}''}} = \sum_{\boldsymbol{k}'\in S(\tilde{\boldsymbol{k}}'')} f(\boldsymbol{k}',\tilde{\boldsymbol{k}}') \sum_{v'c'} (d_{v'\boldsymbol{k}'}^{n_3\tilde{\boldsymbol{k}}'})^* d_{c'\boldsymbol{k}'}^{n_4\tilde{\boldsymbol{k}}'} p_{v'c'\boldsymbol{k}'} \text{ with } \tilde{\boldsymbol{k}}' = \tilde{\boldsymbol{k}''}^{uvw} \tag{37}$$

$$r_{n_1n_2\tilde{\boldsymbol{k}}} = \sum_{\tilde{\boldsymbol{k}}''} \sum_{uvw} \sum_{n_3n_4} K_{n_1n_2\tilde{\boldsymbol{k}},n_3n_4(\tilde{\boldsymbol{k}''}^{uvw})} q^{uvw}_{n_3n_4\tilde{\boldsymbol{k}''}} \tag{38}$$

$$s_{vc\boldsymbol{k}} = \sum_{\tilde{\boldsymbol{k}}\in N(\boldsymbol{k})} f(\boldsymbol{k},\tilde{\boldsymbol{k}}) \sum_{n_1n_2} d_{v\boldsymbol{k}}^{n_1,\tilde{\boldsymbol{k}}}(d_{c\boldsymbol{k}}^{n_2\tilde{\boldsymbol{k}}})^* r_{n_1n_2\tilde{\boldsymbol{k}}}. \tag{39}$$

A schematic representation of the algorithm is given in Fig. 1. The application of the interpolated Hamiltonian is equivalent to averaging dense vector (p) on a coarse vector (q), then applying the coarse Hamiltonian (r) and finally rebuilding the full vector information on the dense mesh (s).

The numerical complexity of Eq. (37), (38) and (39) is $\mathcal{O}(N_c^2N_v^2\tilde{N}_kN_{div})$, $\mathcal{O}(N_c^2N_v^2\tilde{N}_k^2)$, and $\mathcal{O}(N_c^2N_v^2\tilde{N}_kN_{div})$ respectively instead of the $\mathcal{O}(N_c^2N_v^2\tilde{N}_k^2N_{div}^2)$ scaling of a BSE run done on the same dense mesh without interpolation. This first approach is called "Method 1" (M1) in the rest of this work.

As stated at the end of Section 3, a better treatment of the divergence is expected to improve the accuracy of the interpolation. Considering Eq. (30), one

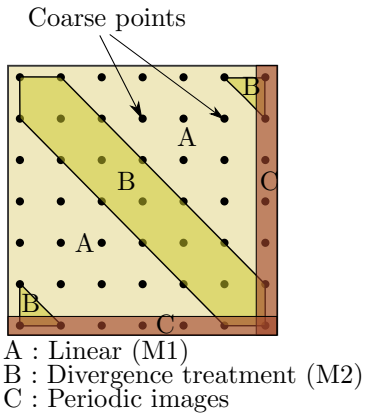

Figure 2: Regions of the Hamiltonian where the interpolation is applied in "Method 3", for a width $w = 1.0$.

can interpolate the coefficients and then divide the interpolated quantities by the $\boldsymbol{q}$ computed on the dense mesh. The drawback of this approach, however, is that it requires the computation of the whole matrix since the fast algorithm developed in Eq. (36) is not applicable thus resulting in $\mathcal{O}(N_c^2 N_v^2 \tilde{N}_k^2 N_{div}^2)$ scaling. This approach is called "Method 2" (M2) in the rest of this work.

The last method ("Method 3", M3) has been developed as a trade-off between accuracy and numerical complexity. In this case, the divergent behavior is reproduced only in a small region along the diagonal with a width that can be adjusted by the user (see Fig. 2). This approximation allows us to employ the fast interpolation of Eq. (36) for the full matrix. The computational cost needed to treat the divergence is negligible provided that the width is small with respect to the number of points on the coarse mesh. Under this assumption, the overall complexity of M3 is $\mathcal{O}(N_c^2 N_v^2 \tilde{N}_k N_{div}^2)$.

We define the width w relatively to the smallest distance between two points in the coarse grid d. Then, all (k, k') pairs in the dense mesh so that $||k - k'|| > w \times d$ are treated with Method 1 and for the other pairs, the coefficients of Eq. (30) are interpolated and used together with the dense $\boldsymbol{q}$ to treat the divergence.

5. Comparison of the interpolation schemes

In this section, the different interpolation schemes are tested and compared in detail. Our method has been implemented in the open source ABINIT code [23, 24] and will be made available in the forthcoming release. First, three different prototype systems, silicon, gallium arsenide and lithium fluoride, are studied and the accuracy of the three schemes discussed in the previous section is studied in detail. Then, a non-physical test case with very low convergence

parameters is used to analyze how the computational cost scales with the total number of points employed to sample the BZ.

5.1. Accuracy on test cases

Silicon and gallium arsenide have relatively high dielectric constant (10.9 for GaAs and 12 for Si [25]) and therefore small binding energies (4-5 meV for GaAs [26, 25] and 15 meV for Si [27]) and Mott-Wannier-like excitons. LiF, on the other hand, has a relatively small dielectric constant of 1.9 [26], yielding a weak screened interaction and therefore strong excitonic effects (binding energy on the order of 3 eV [12, 26, 28, 29]), and Frenkel-like excitons. We decided to use these prototype semi-conductors because, as discussed in [8], their BSE matrices have very different behavior in k-space and it is important to understand how our interpolation scheme performs in two different scenarios.

Si and GaAs have been simulated using cut-off energies of 16 Ha for the wavefunctions and 4 Ha for the dielectric matrix, while for LiF, a cut-off energy of 50 Ha has been used for the wavefunctions and 4 Ha for the dielectric matrix. Three valence bands and four conduction bands were included in the electron-hole basis set. Lanczos chain iterations were stopped when the full dielectric spectrum reached a maximum relative difference of 1% both on the real part and the imaginary part. The model dielectric function of Ref. [22] has been used to avoid the computation of the inverse dielectric matrix, with the parameter ϵ^{∞} set to 12, 10 and 2 for Si, GaAs and LiF respectively. A scissors shift is applied on top of the LDA Kohn-Sham eigenvalues to mimic the effect of the GW approximation (0.8 eV for Si and GaAs, 5.7 eV for LiF). The broadening factor (see Eq. (6)) is $\eta = 0.1$ eV.

Results with two coarse grids of $4 \times 4 \times 4$ and $8 \times 8 \times 8$, interpolated to $8 \times 8 \times 8$ and $16 \times 16 \times 16$, respectively, are presented in Fig. 3, 4 and 5 for silicon, gallium arsenide and lithium fluoride respectively. The three main peak positions and maximum amplitudes extracted from these results are presented in Table. 1, 2 and 3. All the calculations are done with BZ meshes shifted along the $(0.011, 0.021, 0.031)$ direction in order to improve the accuracy of the sampling.

By comparing the interpolation schemes with 8 neighbors (8NB) and standard BSE computations done on the dense mesh, we observe that M1 (8NB) tends to shift the entire spectrum by a small energy and the excitonic binding energy is therefore underestimated. M2 (8NB) and M3 (8NB) give similar results for Si and GaAs that are almost on top of the computation done on the dense mesh. The case of lithium fluoride is more complicated to interpret. In this system, indeed, M1 (8NB) gives inaccurate results for the position of the first exciton (0.2 eV of error for a $8 \times 8 \times 8$ coarse mesh). M2 (8NB) performs better than M1 (8NB) although the error in the position of the first peak is still on the order of 0.12 eV. M3 (8NB) gives the best results: the excitonic binding energy is reproduced with 0.05 eV error and also the behavior at higher frequency is correctly reproduced. It should be stressed, however, that this agreement is somehow fortuitous and related to the particular value of the width w used for

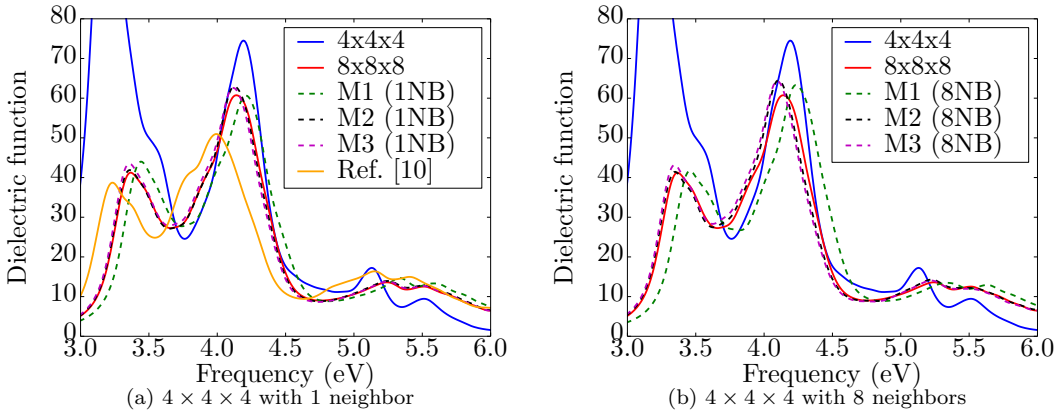

(a) $4 \times 4 \times 4$ with 1 neighbor

(b) $4 \times 4 \times 4$ with 8 neighbors

(c) $8 \times 8 \times 8$ with 1 neighbor

(d) $8 \times 8 \times 8$ with 8 neighbors

Figure 3: (Color online). Comparison between the absorption spectra of silicon obtained with the standard (non-interpolated) BSE solution and with the six levels of interpolation developed in this work. (1NB) refers to the 1-neighbor Rohlfing and Louie technique, whose results are presented in the left column. (8NB) refers to the multilinear technique with 8 neighbors presented in this article, whose results are presented in the right column. Ref. [10] refers to the multiple-shift technique. The results presented in the upper row correspond to the interpolation from the 4x4x4 grid to the 8x8x8 grid, while the lower row corresponds to the interpolation from the 8x8x8 grid to the 16x16x16 grid.

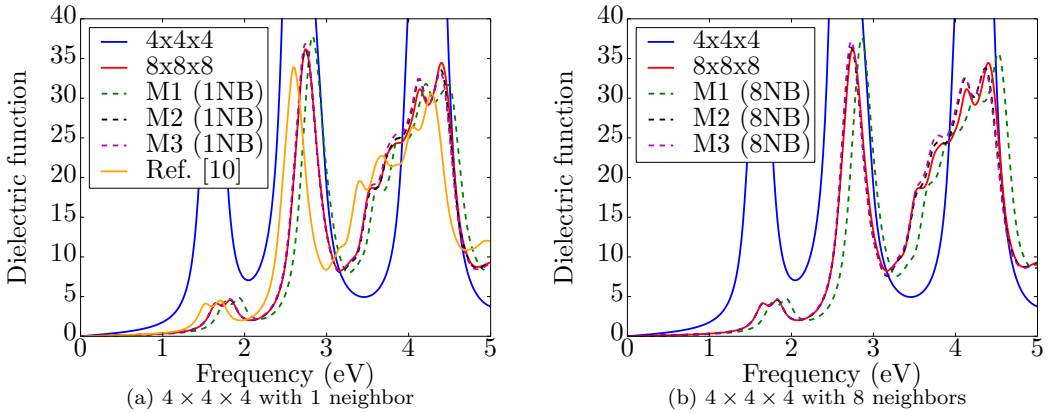

(a) $4 \times 4 \times 4$ with 1 neighbor

(b) $4 \times 4 \times 4$ with 8 neighbors

(c) $8 \times 8 \times 8$ with 1 neighbor

(d) $8 \times 8 \times 8$ with 8 neighbors

Figure 4: (Color online). Comparison between the absorption spectra of gallium arsenide obtained with the standard (non-interpolated) BSE solution and with the six levels of interpolation developed in this work. (1NB) refers to the 1-neighbor Rohlfing and Louie technique, whose results are presented in the left column. (8NB) refers to the multilinear technique with 8 neighbors presented in this article, whose results are presented in the right column. Ref. [10] refers to the multiple-shift technique. The results presented in the upper row correspond to the interpolation from the 4x4x4 grid to the 8x8x8 grid, while the lower row corresponds to the interpolation from the 8x8x8 grid to the 16x16x16 grid.

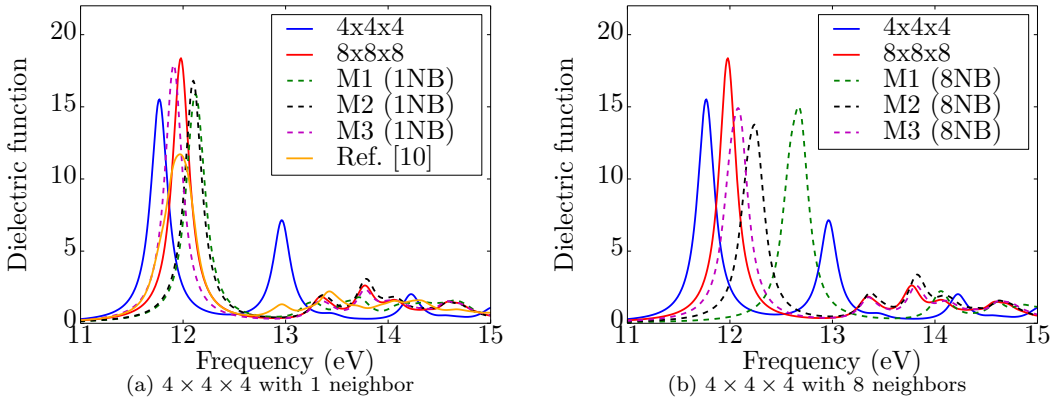

(a) $4 \times 4 \times 4$ with 1 neighbor

(b) $4 \times 4 \times 4$ with 8 neighbors

(c) $8 \times 8 \times 8$ with 1 neighbor

(d) $8 \times 8 \times 8$ with 8 neighbors

Figure 5: (Color online). Comparison between the absorption spectra of lithium fluoride obtained with the standard (non-interpolated) BSE solution and with the six levels of interpolation developed in this work. (1NB) refers to the 1-neighbor Rohlfing and Louie technique, whose results are presented in the left column. (8NB) refers to the multilinear technique with 8 neighbors presented in this article, whose results are presented in the right column. Ref. [10] refers to the multiple-shift technique. The results presented in the upper row correspond to the interpolation from the 4x4x4 grid to the 8x8x8 grid, while the lower row corresponds to the interpolation from the 8x8x8 grid to the 16x16x16 grid.

Method	**Peak I**		**Peak II**		**Peak III**	
	Pos. (eV)	Max.	Pos. (eV)	Max.	Pos. (eV)	Max.
4x4x4	3.19	126.03	4.19	74.53	5.13	17.26
4x4x4 + M1(8NB)	3.46	41.69	4.23	63.32	5.34	13.47
4x4x4 + M2(8NB)	3.35	41.44	4.10	64.31	5.22	14.28
4x4x4 + M3(8NB)	3.35	43.17	4.11	64.50	5.22	14.06
4x4x4 + M1(1NB)	3.44	44.02	4.21	60.66	5.33	14.68
4x4x4 + M2(1NB)	3.36	41.90	4.12	62.59	5.25	13.93
4x4x4 + M3(1NB)	3.36	43.50	4.13	62.93	5.25	13.81
4x4x4 + Ref.[10]	3.23	38.71	3.99	50.97	5.15	16.38
8x8x8	3.37	41.25	4.14	60.74	5.24	13.60
8x8x8 + M1(8NB)	3.55	38.13	4.28	50.99	5.25	14.71
8x8x8 + M2(8NB)	3.51	36.81	4.24	51.58	5.19	15.02
8x8x8 + M3(8NB)	3.51	37.71	4.23	51.56	5.19	14.83
8x8x8 + M1(1NB)	3.55	38.72	4.27	51.00	5.21	14.29
8x8x8 + M2(1NB)	3.51	36.62	4.24	51.05	5.19	14.80
8x8x8 + M3(1NB)	3.51	37.59	4.23	50.98	5.18	14.66
8x8x8 + Ref.[10]	3.58	36.49	4.21	48.34	5.17	14.43
16x16x16	3.50	38.37	4.23	50.80	5.19	14.57

Table 1: Peak position (Pos.) and maximum amplitude (Max.) of the three main peaks of the absorption spectra of silicon represented in Figure 3. See the caption of the figure for a complete description of the notations.

Method	**Peak I**		**Peak II**		**Peak III**	
	Pos. (eV)	Max.	Pos. (eV)	Max.	Pos. (eV)	Max.
4x4x4	1.70	31.67	2.62	104.08	4.34	72.43
4x4x4 + M1(8NB)	1.93	4.75	2.86	37.60	4.52	35.65
4x4x4 + M2(8NB)	1.82	4.62	2.73	36.39	4.37	33.79
4x4x4 + M3(8NB)	1.82	4.67	2.73	37.17	4.36	33.52
4x4x4 + M1(1NB)	1.93	4.85	2.83	37.79	4.48	31.67
4x4x4 + M2(1NB)	1.82	4.62	2.74	36.08	4.39	33.57
4x4x4 + M3(1NB)	1.82	4.67	2.74	36.85	4.39	33.27
4x4x4 + Ref.[10]	1.70	4.53	2.60	33.93	4.28	30.57
8x8x8	1.82	4.57	2.74	36.16	4.40	34.45
8x8x8 + M1(8NB)	2.04	2.95	3.00	25.08	4.47	38.08
8x8x8 + M2(8NB)	2.00	2.83	2.95	24.66	4.42	38.14
8x8x8 + M3(8NB)	2.00	2.87	2.94	25.00	4.41	38.12
8x8x8 + M1(1NB)	2.03	3.12	2.99	25.92	4.45	37.36
8x8x8 + M2(1NB)	1.98	2.88	2.95	25.06	4.42	38.02
8x8x8 + M3(1NB)	1.98	2.91	2.94	25.40	4.41	37.77
8x8x8 + Ref.[10]	1.91	2.69	2.91	23.32	4.38	35.58
16x16x16	1.98	2.95	2.93	25.84	4.41	37.74

Table 2: Peak position (Pos.) and maximum amplitude (Max.) of the three main peaks of the absorption spectra of gallium arsenide represented in Figure 4. See the caption of the figure for a complete description of the notations.

Method	Peak I		Peak II		Peak III	
	Pos. (eV)	Max.	Pos. (eV)	Max.	Pos. (eV)	Max.
4x4x4	11.77	15.52	12.96	7.15	14.22	2.02
4x4x4 + M1(8NB)	12.67	15.02	14.06	2.23	14.61	1.49
4x4x4 + M2(8NB)	12.24	13.77	13.37	2.11	13.83	3.37
4x4x4 + M3(8NB)	12.08	14.92	13.35	1.80	13.82	2.61
4x4x4 + M1(1NB)	12.12	15.88	13.27	1.47	13.72	1.81
4x4x4 + M2(1NB)	12.10	16.82	13.37	1.95	13.79	3.07
4x4x4 + M3(1NB)	11.91	17.91	13.35	1.57	13.78	2.34
4x4x4 + Ref.[10]	11.97	11.71	12.96	1.32	13.43	2.21
8x8x8	12.0	18.4	13.35	1.85	13.77	2.62
8x8x8 + M1(8NB)	12.20	18.00	13.88	3.04	14.21	1.75
8x8x8 + M2(8NB)	12.12	16.52	13.56	3.46	14.00	1.72
8x8x8 + M3(8NB)	11.95	17.80	13.54	3.05	14.00	1.51
8x8x8 + M1(1NB)	12.02	18.06	13.52	2.68	13.72	1.81
8x8x8 + M2(1NB)	12.07	17.16	13.54	3.53	13.99	1.65
8x8x8 + M3(1NB)	11.90	18.31	13.51	3.34	13.86	1.47
8x8x8 + Ref.[10]	11.98	18.39	13.47	2.23	13.77	1.62
16x16x16	11.99	18.49	13.52	3.22	13.99	1.51

Table 3: Peak position (Pos.) and maximum amplitude (Max.) of the three main peaks of the absorption spectra of lithium fluoride represented in Figure 5. See the caption of the figure for a complete description of the notations.

the treatment of the divergence. Figure 6 shows the optical spectra of LiF computed with M3 and different values of w. Our results indicate that the value of the width used in M3 has a significant impact on the position of the first peak of LiF. Therefore some sort of convergence study is needed for M3 in order to find values of w giving a good compromise between accuracy and efficiency.

If we compare the method using one neighbor (1NB) and the eight neighbors (8NB), we observe that the original Rohlfing and Louie interpolation (1NB) gives results for GaAs and Si whose quality is comparable to the multilinear interpolation and even better results for the special case of LiF. This is somehow puzzling and our current understanding is as follows. As already mentioned in the previous paragraph, the description of the divergent behavior along the diagonal of the Hamiltonian for LiF is extremely important to get a correct binding energy. In practice, the number of bands used in Eq. (20) must be truncated and therefore the expansion is not exact. Furthermore, we neglect in the expansion possible contributions to valence (conduction) states coming from the conduction (valence) manifold in Eq. (24). This approximation is also used in Ref. [5]. Some terms are therefore neglected and they lead to some loss of information when building the interpolated matrix element from multiple neighbors.

Our results indicate that, although the multilinear interpolation was expected to give more accurate results, the practical implementation and the numerical approximations tend to favor a "simple" 1-neighbor interpolation.

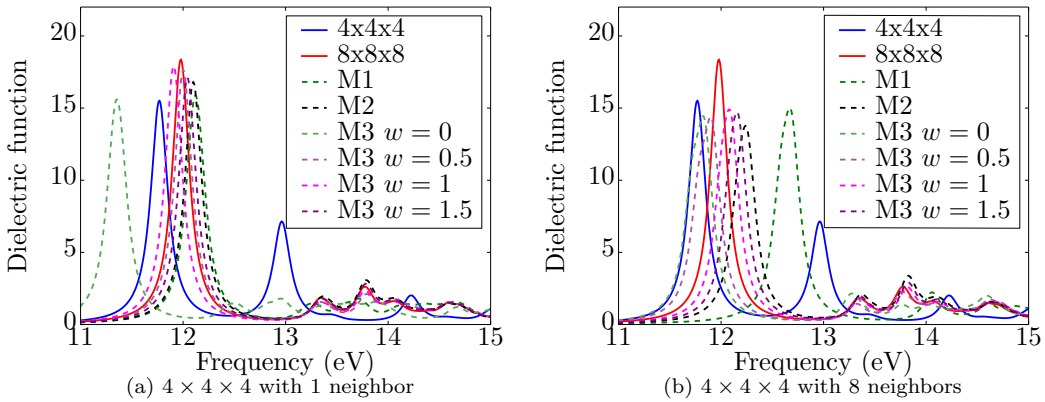

(a) $4 \times 4 \times 4$ with 1 neighbor

(b) $4 \times 4 \times 4$ with 8 neighbors

Figure 6: (Color online). Optical absorption spectrum of LiF obtained with different values of the width w used for the treatment of the divergence.

This interpolation gives sufficient accuracy at a lower computational cost as summations over 1 neighbor are cheaper than summations over 8 neighbors.

For the sake of completeness, we have also compared our methods with the multiple-shift technique introduced in Ref. [6, 10] and used recently in Ref. [8]. Different coarse grids are obtained by shifting an initial homogeneous mesh so that the full set of points forms a much denser sampling. An approximate dielectric function is then obtained by averaging the results obtained on the coarse grids. As can be seen in Fig. 3, 4 and 5, this technique tends to smooth the spectrum and the amplitude of the peaks is underestimated. As stated in Ref. [8], due to the localized character of the exciton in LiF, a small number of points in the coarse grids is enough to converge the peak position but the correct description of the fine details of the spectrum requires more accurate methods. The methods developed in the present article are more accurate than this technique and are significantly cheaper as they do not require multiple expensive calculations of BSE Hamiltonians.

As regards computational efficiency, one should notice that the time required to produce an interpolated spectrum for LiF in sequential with the above-mentioned parameters is respectively 22200 sec for M1 (8NB), 120000 sec for M2 (8NB), 3000 sec for M1 (1NB) and 80000 sec for M2 (1NB). As a reference, the time needed to compute the matrix elements of the BSE Hamiltonian on the coarse mesh is around 15000 sec and around 1×10^6 sec for the dense mesh. To sum up, M1 leads to a gain of two orders of magnitude in terms of CPU time while the high-accuracy M2 gives a speedup of one order of magnitude. The memory required by M1 is of the same order as the one needed for a calculation on the coarse mesh whereas M2 is much more memory demanding since the whole dense matrix must be stored.

The technique based on multiple shifts, on the other hand, requires 8 cal-

	`Matmul`	`Hinterp`
M1	$\mathcal{O}(\tilde{N}_k^2 + \tilde{N}_k N_{div})$	-
M2	$\mathcal{O}(\tilde{N}_k^2 N_{div}^2)$	$\mathcal{O}(\tilde{N}_k^2 N_{div}^2)$
M3	$\mathcal{O}(\tilde{N}_k N_{div}^2 + \tilde{N}_k^2)$[*]	$\mathcal{O}(\tilde{N}_k N_{div}^2)$

Table 4: Theoretical scalings of the routines used in the three methods described in the text. [*] Scaling of an optimal implementation that takes advantage of sparse matrices. The scaling becomes $\mathcal{O}(\tilde{N}_k^2 N_{div}^2)$ if the method is solved with dense matrices.

culations of a coarse Hamiltonian. These calculations are independent and can be executed in parallel but the final results cannot reach the same frequency resolution as the ones obtained with a fast interpolation on a dense k-mesh.

5.2. Numerical scaling of the interpolation technique

In order to assess the numerical scaling of our implementation, we have performed several benchmarks for silicon with unconverged parameters. A cut-off energy of 4 Ha has been used for the wavefunctions and 2 Ha for the dielectric function. Only one valence and one conduction band are included in the Bethe-Salpeter kernel. This allowed us to increase the number of wavevectors of the dense grid to more than 100000 wavevectors in the BZ.

For the three different methods, we have analyzed the time spent in the most important routines. Different benchmarks have been performed by changing the initial coarse grid as well as the final dense mesh of $\tilde{N}_k \times N_{div}$ wavevectors. The most CPU-critical sections are `Hinterp` for the calculation of the interpolated matrix elements and `Matmul` for the matrix-vector multiplications needed for the Lanczos method. The theoretical scaling is given in Table 4 while the results of the tests are reported in Fig. 7. Several interesting observations on the major trends can be derived from the benchmarks. If we look at the interpolated matrix-vector product (`Matmul`), we observe that M1 is very efficient as it scales with the square of the size of the coarse mesh. On the other hand, both M2 and M3 are less performant. Finally, the time spent by M3 in the routine `Hinterp` (interpolation of matrix elements) is much smaller than the one spent by M2 at dense meshes.

5.3. Comparison with the Kammerlander double-grid technique

In this section, we compare our method with the technique proposed by Kammerlander in Ref. [16]. In this approach, the polarizability $L(\omega)$ is expressed in the transition space according to

$$L_{vc\boldsymbol{k},v'c'\boldsymbol{k}'}(\omega) = \sum_{v''c''\boldsymbol{k}''} (1 - L^0(\omega)K)^{-1}_{vc\boldsymbol{k},v''c''\boldsymbol{k}''} L^0_{v''c''\boldsymbol{k}'',v'c'\boldsymbol{k}'}(\omega), \tag{40}$$

where the RPA polarizability $L^0(\omega)$ is given by

$$L^0_{vc\boldsymbol{k},v'c'\boldsymbol{k}'}(\omega) = \frac{f_{c\boldsymbol{k}} - f_{v\boldsymbol{k}}}{\varepsilon_{c\boldsymbol{k}} - \varepsilon_{v\boldsymbol{k}} - \omega - i\eta} \delta_{cc'} \delta_{vv'} \delta_{\boldsymbol{k},\boldsymbol{k}'}. \tag{41}$$

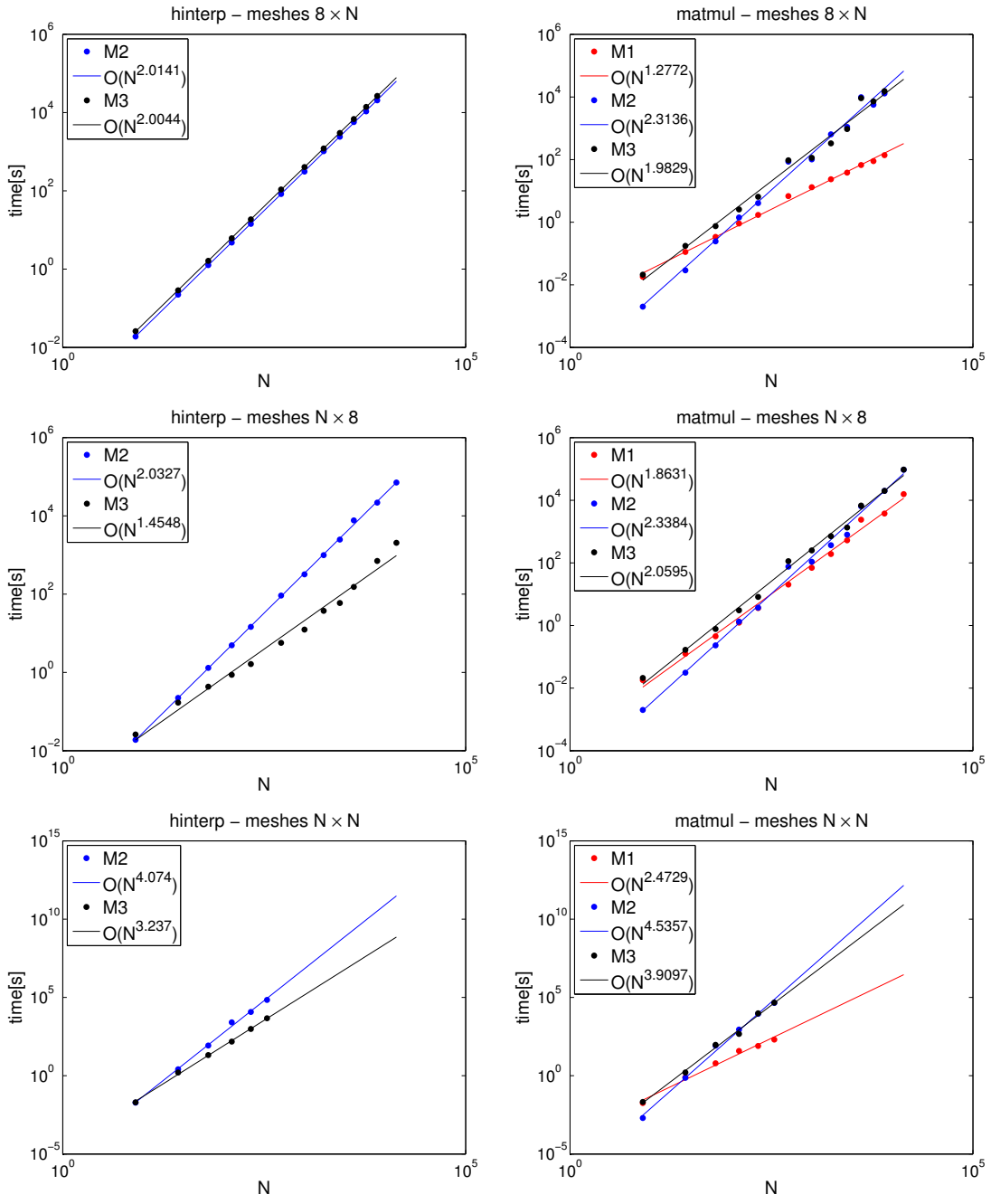

Figure 7: Measured scaling for the three interpolation methods

In order to avoid the direct inversion of the large matrix, an iterative scheme is used for the computation of

$$L_{vc\boldsymbol{k},v'c'\boldsymbol{k}'}(\omega) = \sum_m \sum_{v''c''\boldsymbol{k}''} \left[L^0(\omega)K\right]^m_{vc\boldsymbol{k},v''c''\boldsymbol{k}''} L^0_{v''c''\boldsymbol{k}'',v'c'\boldsymbol{k}'}(\omega). \tag{42}$$

The BSE is solved for every frequency in an iterative way and a double grid technique is used to reduce the number of k-points for which the kernel must be computed explicitly. The RPA polarizability is averaged on a dense mesh yielding

$$L^0_{vc\boldsymbol{k},v'c'\boldsymbol{k}'}(\omega) = \frac{1}{N_{nb}} \sum_{\bar{\boldsymbol{k}}\in N(\boldsymbol{k})} \frac{f_{c\bar{\boldsymbol{k}}} - f_{v\bar{\boldsymbol{k}}}}{\varepsilon_{c\bar{\boldsymbol{k}}} - \varepsilon_{v\bar{\boldsymbol{k}}} - \omega - i\eta} \delta_{cc'}\delta_{vv'}\delta_{\boldsymbol{k},\boldsymbol{k}'}, \tag{43}$$

where the $\bar{\boldsymbol{k}}$ are taken from the set $N(\boldsymbol{k})$ of N_{nb} dense points located around $\boldsymbol{k}$.

Finally the averaged values are used in the iterative BSE solver [see Eq. (42)]. This approach has the advantage that the wavefunctions on the dense mesh are not needed but the divergence is not accurately reproduced. The scaling of the Kammerlander technique is linear with the number of frequencies and quadratic with the number of points in the coarse mesh. On the contrary, our technique is able to describe the frequency dependence with a computational cost that does not depend on the number of frequency points, since, as discussed in Section 2, $\varepsilon_M(\omega)$ is evaluated with Eq. (13) whose cost is negligible.

5.4. Wavefunction interpolation

In this article, we assume that the entire set of wavefunctions on the dense set of points is available. For the systems investigated in this study, the calculation of wavefunctions starting from an already converged density is not the most computationally demanding part. Moreover, only wavefunctions in the transition basis set are required, that is a small fraction of the set of bands required for the screening, for example.

However, for some more complex systems, one might take advantage of interpolation techniques to obtain the wavefunctions on denser meshes. In the work of Kammerlander [16] presented in the previous section, Wannier functions were used to obtain eigenenergies on these dense meshes. Recently, Gilmore *et al.* [30] have used optimized basis functions described in the work of Shirley [31] to compute wavefunctions on a dense mesh. These different techniques could be easily interfaced with our technique to compute the overlap matrix elements, that can afterwards be used in the interpolation of the BSE Hamiltonian.

6. Conclusions

We have presented a fast and memory-efficient technique that combines the interpolation of the Bethe-Salpeter matrix elements with the Lanczos algorithm. The treatment of the matrix elements is similar in spirit to the Rohlfing and

Louie approach but we avoid the storage and the diagonalization of large matrices. Three possible approaches for the treatment of the Coulomb singularity have been presented and discussed in detail.

The effectiveness of the method has been analyzed through calculations of optical spectral in Si, GaAs and LiF. According to our tests, the multilinear interpolation of the wavefunctions does not perform better than simple constant interpolation, already proposed by Rohlfing and Louie (although used by them only for the set up of the Hamiltonian on the dense mesh).

In conclusion, we suggest using Method 1 for a quick qualitative analysis of optical spectra e.g. for a high-throughput screening to rapidly identify possible candidates. Method 3 with the on-the-fly interpolation is the recommended approach for BSE calculations requiring dense k-meshes since it is significantly faster than M2 and the Coulomb divergence is taken into account. The downside is that one has to check the convergence with the width w, but we believe this is a small price to pay, especially when compared with the significant speedup that can be achieved.

The algorithmic improvements presented in this work will facilitate BSE calculations in complex systems and will also significantly ease the ab initio study of piezoreflectance, thermoreflectance and Raman intensities in systems with excitonic effects.

7. Acknowledgments

Y.G. and M.G. wish to acknowledge the financial support of the Fonds National de la Recherche Scientifique (FNRS, Belgium). The authors would like to thank Yann Pouillon and Jean-Michel Beuken for their valuable technical support and help with the test and build system of ABINIT.

Computational resources have been provided by the supercomputing facilities of the Université catholique de Louvain (CISM/UCL) and the Consortium des Equipements de Calcul Intensif en Fédération Wallonie Bruxelles (CECI) funded by the Fonds de la Recherche Scientifique de Belgique (FRS-FNRS) under Grant No. 2.5020.11. This work was also supported by the FRS-FNRS Belgium through PDR Grant T.0238.13 - AIXPHO.

8. References

[1] G. Onida, L. Reining, A. Rubio, Electronic excitations: density-functional versus many-body Green's-function approaches, Rev. Mod. Phys. 74 (2002) 601–659. doi:10.1103/RevModPhys.74.601.
URL http://link.aps.org/doi/10.1103/RevModPhys.74.601

[2] S. Albrecht, L. Reining, R. Del Sole, G. Onida, *Ab Initio* calculation of excitonic effects in the optical spectra of semiconductors, Phys. Rev. Lett. 80 (1998) 4510–4513. doi:10.1103/PhysRevLett.80.4510.
URL http://link.aps.org/doi/10.1103/PhysRevLett.80.4510

[3] G. Kresse, M. Marsman, L. E. Hintzsche, E. Flage-Larsen, Optical and electronic properties of Si_3N_4 and α-SiO_2, Phys. Rev. B 85 (2012) 045205. doi:10.1103/PhysRevB.85.045205.
URL http://link.aps.org/doi/10.1103/PhysRevB.85.045205

[4] P. Rinke, A. Schleife, E. Kioupakis, A. Janotti, C. Rödl, F. Bechstedt, M. Scheffler, C. G. Van de Walle, First-principles optical spectra for F centers in MgO, Phys. Rev. Lett. 108 (2012) 126404. doi:10.1103/PhysRevLett.108.126404.
URL http://link.aps.org/doi/10.1103/PhysRevLett.108.126404

[5] M. Rohlfing, S. G. Louie, Electron-hole excitations and optical spectra from first principles, Phys. Rev. B 62 (2000) 4927–4944. doi:10.1103/PhysRevB.62.4927.
URL http://link.aps.org/doi/10.1103/PhysRevB.62.4927

[6] J. Paier, M. Marsman, G. Kresse, Dielectric properties and excitons for extended systems from hybrid functionals, Phys. Rev. B 78 (2008) 121201. doi:10.1103/PhysRevB.78.121201.
URL http://link.aps.org/doi/10.1103/PhysRevB.78.121201

[7] M. Grüning, A. Marini, X. Gonze, Implementation and testing of lanczos-based algorithms for Random-Phase approximation eigenproblems, Comp. Mater. Sci. 50 (7) (2011) 2148–2156. doi:10.1016/j.commatsci.2011.02.021.
URL http://linkinghub.elsevier.com/retrieve/pii/S092702561100111X

[8] T. Sander, E. Maggio, G. Kresse, Beyond the Tamm-Dancoff approximation for extended systems using exact diagonalization, Phys. Rev. B 92 (2015) 045209. doi:10.1103/PhysRevB.92.045209.
URL http://link.aps.org/doi/10.1103/PhysRevB.92.045209

[9] A. Marini, *Ab Initio* finite-temperature excitons, Phys. Rev. Lett. 101 (2008) 106405. doi:10.1103/PhysRevLett.101.106405.
URL http://link.aps.org/doi/10.1103/PhysRevLett.101.106405

[10] Y. Gillet, M. Giantomassi, X. Gonze, First-principles study of excitonic effects in raman intensities, Phys. Rev. B 88 (2013) 094305. doi:10.1103/PhysRevB.88.094305.
URL http://link.aps.org/doi/10.1103/PhysRevB.88.094305

[11] R. Haydock, The recursive solution of the Schrödinger equation, Comput. Phys. Comm. 20 (1) (1980) 11 – 16. doi:10.1016/0010-4655(80)90101-0.
URL http://www.sciencedirect.com/science/article/pii/0010465580901010

[12] L. X. Benedict, E. L. Shirley, R. B. Bohn, Optical absorption of insulators and the electron-hole interaction: An *Ab Initio* calculation, Phys. Rev.

Lett. 80 (1998) 4514–4517. doi:10.1103/PhysRevLett.80.4514.
URL http://link.aps.org/doi/10.1103/PhysRevLett.80.4514

[13] L. X. Benedict, E. L. Shirley, Ab initio calculation of $\epsilon_2(\omega)$ including the electron-hole interaction: Application to GaN and CaF_2, Phys. Rev. B 59 (1999) 5441–5451. doi:10.1103/PhysRevB.59.5441.
URL http://link.aps.org/doi/10.1103/PhysRevB.59.5441

[14] J. Deslippe, G. Samsonidze, D. A. Strubbe, M. Jain, M. L. Cohen, S. G. Louie, Berkeleygw: A massively parallel computer package for the calculation of the quasiparticle and optical properties of materials and nanostructures, Computer Physics Communications 183 (6) (2012) 1269 – 1289. doi:http://dx.doi.org/10.1016/j.cpc.2011.12.006.
URL http://www.sciencedirect.com/science/article/pii/S0010465511003912

[15] F. Fuchs, C. Rödl, A. Schleife, F. Bechstedt, Efficient $\mathcal{O}(N^2)$ approach to solve the Bethe-Salpeter equation for excitonic bound states, Phys. Rev. B 78 (2008) 085103. doi:10.1103/PhysRevB.78.085103.
URL http://link.aps.org/doi/10.1103/PhysRevB.78.085103

[16] D. Kammerlander, S. Botti, M. A. L. Marques, A. Marini, C. Attaccalite, Speeding up the solution of the Bethe-Salpeter equation by a double-grid method and wannier interpolation, Phys. Rev. B 86 (2012) 125203. doi:10.1103/PhysRevB.86.125203.
URL http://link.aps.org/doi/10.1103/PhysRevB.86.125203

[17] M. Grüning, A. Marini, X. Gonze, Exciton-Plasmon states in nanoscale materials: Breakdown of the Tamm-Dancoff approximation, Nano Letters 9 (8) (2009) 2820–2824. doi:10.1021/nl803717g.
URL http://pubs.acs.org/doi/abs/10.1021/nl803717g

[18] P. Hohenberg, W. Kohn, Inhomogeneous electron gas, Phys. Rev. 136 (1964) B864–B871. doi:10.1103/PhysRev.136.B864.
URL http://link.aps.org/doi/10.1103/PhysRev.136.B864

[19] W. Kohn, L. J. Sham, Self-consistent equations including exchange and correlation effects, Phys. Rev. 140 (1965) A1133–A1138. doi:10.1103/PhysRev.140.A1133.
URL http://link.aps.org/doi/10.1103/PhysRev.140.A1133

[20] S. L. Adler, Quantum theory of the dielectric constant in real solids, Phys. Rev. 126 (1962) 413–420. doi:10.1103/PhysRev.126.413.
URL http://link.aps.org/doi/10.1103/PhysRev.126.413

[21] N. Wiser, Dielectric constant with local field effects included, Phys. Rev. 129 (1963) 62–69. doi:10.1103/PhysRev.129.62.
URL http://link.aps.org/doi/10.1103/PhysRev.129.62

[22] G. Cappellini, R. Del Sole, L. Reining, F. Bechstedt, Model dielectric function for semiconductors, Phys. Rev. B 47 (1993) 9892–9895. doi:10.1103/PhysRevB.47.9892.
URL http://link.aps.org/doi/10.1103/PhysRevB.47.9892

[23] X. Gonze, G.-M. Rignanese, M. Verstraete, J.-M. Beuken, Y. Pouillon, R. Caracas, F. Jollet, M. Torrent, G. Zerah, M. Mikami, G. Ph., J.-Y. Veithen, M.and Raty, V. Olevano, F. Bruneval, L. Reining, R. Godby, G. Onida, D. Hamann, D. Allan, A brief introduction to the abinit software package, Z. Kristallogr. 220 (2005) 558.
URL http://www.oldenbourg-link.com/doi/abs/10.1524/zkri.220.5.558.65066

[24] X. Gonze, B. Amadon, P.-M. Anglade, J. Beuken, F. Bottin, P. Boulanger, F. Bruneval, D. Caliste, R. Caracas, M. Côté, T. Deutsch, L. Genovese, P. Ghosez, M. Giantomassi, S. Goedecker, H. Hamann, P. Hermet, F. Jollet, G. Jomard, S. Leroux, M. Mancini, S. Mazevet, M. Oliveira, G. Onida, Y. Pouillon, T. Rangel, G.-M. Rignanese, D. Sangalli, R. Shaltaf, M. Torrent, M. Verstraete, G. Zerah, J. W. Zwanziger, Abinit : First-principles approach of materials and nanosystem properties, Comput. Phys. Comm. 180 (2009) 2582.
URL http://www.sciencedirect.com/science/article/pii/S0010465509002276

[25] P. Y. Yu, M. Cardona, Fundamentals of Semiconductors: Physics and Material Properties, Springer, 2010.

[26] M. Rohlfing, S. G. Louie, Electron-hole excitations in semiconductors and insulators, Phys. Rev. Lett. 81 (1998) 2312–2315. doi:10.1103/PhysRevLett.81.2312.
URL http://link.aps.org/doi/10.1103/PhysRevLett.81.2312

[27] M. A. Green, Improved value for the silicon free exciton binding energy, AIP Advances 3 (11) (2013) –. doi:http://dx.doi.org/10.1063/1.4828730.
URL http://scitation.aip.org/content/aip/journal/adva/3/11/10.1063/1.4828730

[28] B. Arnaud, M. Alouani, Local-field and excitonic effects in the calculated optical properties of semiconductors from first-principles, Phys. Rev. B 63 (2001) 085208. doi:10.1103/PhysRevB.63.085208.
URL http://link.aps.org/doi/10.1103/PhysRevB.63.085208

[29] A. Marini, R. Del Sole, A. Rubio, Bound excitons in time-dependent density-functional theory: Optical and energy-loss spectra, Phys. Rev. Lett. 91 (2003) 256402. doi:10.1103/PhysRevLett.91.256402.
URL http://link.aps.org/doi/10.1103/PhysRevLett.91.256402

[30] K. Gilmore, J. Vinson, E. Shirley, D. Prendergast, C. Pemmaraju, J. Kas, F. Vila, J. Rehr, Efficient implementation of core-excitation Bethe-Salpeter equation calculations, Computer Physics Communications 197 (2015) 109 – 117. doi:http://dx.doi.org/10.1016/j.cpc.2015.08.014.
URL http://www.sciencedirect.com/science/article/pii/S0010465515003008

[31] E. L. Shirley, Optimal basis sets for detailed Brillouin-zone integrations, Phys. Rev. B 54 (1996) 16464–16469. doi:10.1103/PhysRevB.54.16464.
URL http://link.aps.org/doi/10.1103/PhysRevB.54.16464